

Jitter Measurements of 1 cm² LGADs for Space Experiments

Ashish Bisht ^{1,*} , Leo Cavazzini ^{1,2,*} , Matteo Centis Vignali ¹ , Fabiola Caso ^{1,3}, Omar Hammad Ali ¹ ,
Francesco Ficorella ¹ , Maurizio Boscardin ¹  and Giovanni Paternoster ¹ 

¹ Fondazione Bruno Kessler, Via Sommarive 18, Povo, 38123 Trento, Italy; mcentisvignali@fbk.eu (M.C.V.); fabiola.caso@studenti.unitn.it (F.C.); ohammadali@fbk.eu (O.H.A.); ficorella@fbk.eu (F.F.); boscardin@fbk.eu (M.B.); paternoster@fbk.eu (G.P.)

² Department of Physics, University of Trento, Via Sommarive 14, 38123 Trento, Italy

³ Industrial Engineering Department, University of Trento, Via Sommarive 9, 38123 Trento, Italy

* Correspondence: abisht@fbk.eu (A.B.); leo.cavazzini@unitn.it (L.C.)

Abstract: This work explores the possibility of using Low Gain Avalanche Diodes (LGADs) for tracker-based experiments studying Charged Cosmic Rays (CCRs) in space. While conventional silicon microstrip sensors provide only spatial information about the charged particle passing through the tracker, LGADs have the potential to provide additional timing information with a resolution in the order of tens of picoseconds. For the first time, it has been demonstrated that an LGAD with an active area of approximately 1 cm² can achieve a jitter of less than 40 ps. A comparison of design and gain layers is carried out to understand which provides the best time resolution. For this purpose, laboratory measurements of sensors' electrical properties and gain using LED and an Infrared laser, as well as their jitter, were performed.

Keywords: silicon detectors; LGADs; jitter; astroparticle detectors in space; charged-particle tracking



Citation: Bisht, A.; Cavazzini, L.; Centis Vignali, M.; Caso, F.; Hammad Ali, O.; Ficorella, F.; Boscardin, M.; Paternoster, G. Jitter Measurements of 1 cm² LGADs for Space Experiments. *Instruments* **2024**, *8*, 27. <https://doi.org/10.3390/instruments8020027>

Academic Editor: Antonio Ereditato

Received: 1 March 2024

Revised: 23 March 2024

Accepted: 27 March 2024

Published: 29 March 2024



Copyright: © 2024 by the authors. Licensee MDPI, Basel, Switzerland. This article is an open access article distributed under the terms and conditions of the Creative Commons Attribution (CC BY) license (<https://creativecommons.org/licenses/by/4.0/>).

1. Introduction

Many space missions are currently operating in space to observe and measure the flux of Charged Cosmic Rays (CCRs) [1–6]. These experiments feature a combination of a calorimeter and a tracker [7] to measure the charge magnitude, charge sign, momentum, energy, and velocity of incoming charged particles. However, a challenge can arise in reconstructing the charged particles due to the background introduced by the back-scattered secondary particles from the calorimeter. This background worsens with the increase in the energy of the incoming particles. Most of the tracker systems in these experiments use solid-state detectors, for which the energy deposited by the primary particles cannot be separated from the energy deposited by the back-scattered secondaries. However, it has been shown that measuring the timing of charged particles crossing the tracker layers with a precision better than 100 ps can help separate the primary from the secondary particles [8]. In particular, integrating timing information into silicon trackers enhances the tracker reconstruction capabilities of CCRs in space by introducing extra coordinates to the phase space and also helps in distinguishing between hadronic and electromagnetic showers produced within the calorimeter [8]. Furthermore, it can solve issues such as “ghost hits” and pile-ups commonly occurring in trackers using strip sensors [9].

In the last decade, Low Gain Avalanche Diodes (LGADs) have emerged as efficient time-tagging detectors for High-Energy Physics (HEP) experiments. The LGADs are silicon detectors with an internal gain of $\mathcal{O}(10)$, capable of achieving a timing resolution of $\sigma \sim 30$ ps [10,11]. A schematic sketch of an LGAD with its electric field profile is shown in Figure 1. The typical active area of the sensors used in HEP experiments is of the order of $\mathcal{O}(1 \text{ mm}^2)$, with a thickness of 50 μm , whereas working experiments such as AMS [7] or DAMPE [6], as well as planned experiments such as AMS-100 [12], use silicon micro-strip sensors for tracking, which have 60–100 cm channels with 100–200 μm pitch, resulting

in a channel size of approximately 1 cm^2 . To ensure good timing capabilities, the sensor must have minimum intrinsic noise, while keeping the slew rate of the output signal as high as possible, to reduce the jitter contribution. An increase in the area implies a larger volume of current in the sensor and a higher capacitance, with increased noise and reduced bandwidth. With this in mind, the capacitance of an LGAD with 1 cm^2 active area is 100 times higher than the ones used for HEP with the same thickness. As a consequence, worse timing performances are expected for LGADs with large areas.

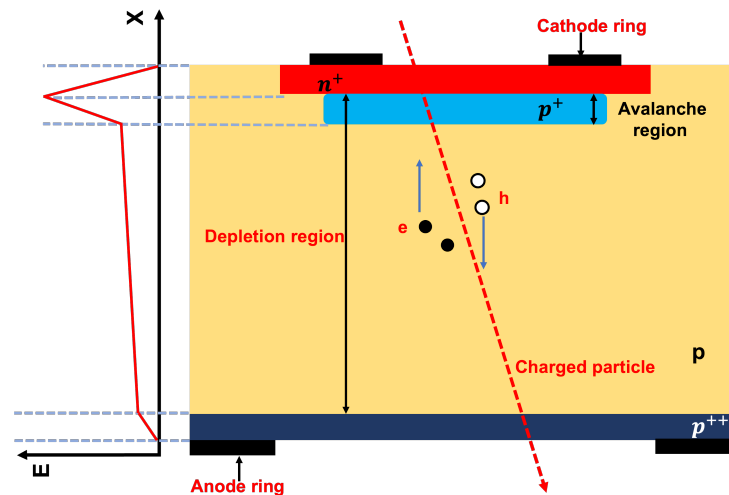


Figure 1. Cross-section of a standard LGAD sensor along with the electric field strength as a function of sensor thickness. The peak of the electric field corresponds to the gain region where charge carriers experience multiplication. Figure adapted from [13].

This work aims to prove that it is possible to produce LGADs with areas in the order of 1 cm^2 to realize timing detectors in space-based experiments by tuning the gain and the device's thickness. The paper is structured as follows. In Section 2, the LTspice simulation that helped in identifying the thickness and gain range to be explored is discussed. The fabrication of sensors with their process parameters is described in Section 3. Later, in Section 4, the measurements of the produced sensors are presented, including electrical characterizations and laboratory measurements with an infrared laser. Finally, Section 5 summarizes the main results obtained with this study.

2. Scaling Channel Size: LTspice Simulation

To assess the expected performance of LGADs with an area of 1 cm^2 , an LTspice [14] simulation was performed to estimate the jitter for different combinations of gain and thickness when the channel size is increased from 1 mm^2 to 1 cm^2 .

From the simulation, two crucial parameters of the sensors are used as figures of merit: the slew rate and the jitter. The slew rate was calculated by determining the ratio between the amplitude and the signal peaking time. The peaking time refers to the time it takes for the signal to reach its maximum level after charge carrier generation in the sensor. The slew rate was then used to determine the jitter of the sensor by dividing the noise for it. The signal is determined assuming saturated drift velocities in the whole sensor thickness. The initial ionization is assumed to be uniform along the sensor thickness, and its magnitude is given by the Most Probable Value (MPV) of the energy deposition of a minimum ionizing particle. The MPV scales with the sensor thickness according to [15]. The assumption of a uniform distribution of the initial ionization excludes the Landau term of the time resolution; therefore, only the jitter of the sensor is calculated. The signal shape is modeled accounting for the drift of the primary ionization electrons and holes and the multiplication holes. The current pulse is then shaped by the RC circuit formed by the sensor capacitance and the impedance of the input of the readout electronics. The noise contribution of the sensor is restricted to the shot noise. The shot noise is calculated

considering the bulk generation current of the sensor, with a generation per unit volume determined by a previous LGAD batch. The shot noise is then calculated accounting for the multiplication (M) and excess noise factors (F) and the bandwidth of the RC circuit. The values of F are, for the sake of simplicity, assumed to scale with M, with the value of $F = 3$ for $M = 10$ referring to [16]. Finally, the noise of the readout electronics is assumed to be constant for all conditions and fixed at $0.4 \mu\text{A}$, typical of commercial broadband amplifiers [17]. The simulation parameters are reported in Table 1. Since the peaking time is used, the value of the slew rate represents an average over the signal leading edge, which will result in an overestimation of the jitter of the sensors because points with a larger slew rate can be used to determine the time of arrival of particles.

Table 1. Simulation parameters considered for the scaling of LGAD channel size. The excess noise factor is the additional noise arising due to the stochastic nature of the impact ionization process [18].

Area (cm ²)	Gain (M)	Excess Noise Factor (F)
0.01	10	3
	20	6
1	10	3
	100	30
	500	150

Figure 2 illustrates the correlation between sensor thickness, slew rate, and jitter values. For a given sensor area, the slew rate increases with higher gain values, while the shot noise remains unaffected by the active area, depending only on the sensor thickness, gain, and excess noise factor. Therefore, the jitter decreases with increasing gain values for a given electronic noise level. Jitter values below 50 ps can be achieved for a channel size of 1 cm^2 , having a sensor thickness above $100 \mu\text{m}$ and a gain around 100.

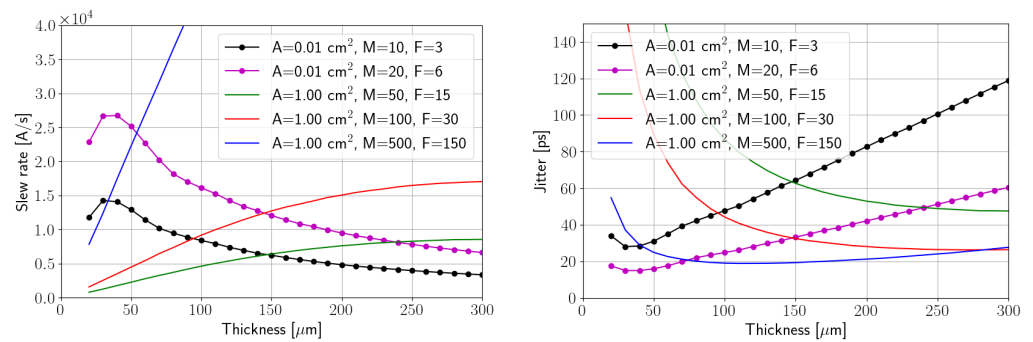


Figure 2. LTspice simulations of slew rate (left) and jitter (right) as a function of the sensor thickness, for different gain (M) and the excess noise (F). The black and purple markers represent the standard LGADs used in HEP.

To obtain the best timing performance, the drift velocities of the charge carriers must be saturated. This requires an electric field of approximately 20 kV/cm [19] to be present in the whole thickness of the sensor. To achieve this condition, a bias voltage of 100, 200, and 300 V must be added on top of the depletion voltage for 50, 100, and $150 \mu\text{m}$ -thick sensors, respectively, determining the operation point of the sensors. For the current work, a bias of approximately 100 V is considered to be sufficient for the depletion of the gain layer and the bulk at any of the thicknesses mentioned above, resulting in a desired gain of 100 at 400 V bias for $150 \mu\text{m}$ -thick sensors. A further increase in sensor thickness would require an increase in the bias voltage for both the sensor depletion (which grows quadratically with thickness for a given resistivity) and for the drift velocity saturation (which grows linearly with thickness). The thermal generation current also scales linearly with the sensor thickness for a given area and together with the bias voltage determines the sensor power

consumption. As space experiments can have strong constraints in their power budget, limiting the power consumption of the sensors is a desirable feature.

Another challenge of scaling up the channel size is to avoid non-uniformities in the signal shape when particles traverse the sensor at different positions over the channel area. A possible source of this non-uniformity can be the resistivity of the n^+ layer through which the signal propagates towards the readout electronics. The design of the sensor metallization and the positions at which it contacts the n^+ layer can help in reducing this effect by providing a low impedance path between the particle impact position and the readout electronics.

The choice of the fabrication parameters of the sensors is guided by Technology Computer-Aided Design (TCAD) simulations [20] that were performed to optimize the gain layer of the LGADs for the working points discussed above [21]. The fabrication parameters are summarized in Table 2. The gain layer dose is varied around the points indicated by the simulation to account for possible uncertainties in the simulation models. The thickness of the sensors was constrained by the available starting material, and the 50 μm sensors are present as a reference since this thickness is commonly used in HEP applications.

Table 2. Normalized process parameters used in the fabrication of SLAPP batch.

Thickness (μm)	Wafer	n^+ Dose	Gain Dose	Gain Energy
50	1	1	0.98	1
	2	1	1	1
	3	3	1	1
	4	3	0.98	1
100	5	1	1.04	1
	6	1	1.08	1
	7	1	1.12	1
	8	1	1.4	0.5
	9	1	1.46	0.5
	10	1	1.52	0.5
150	11	1	1.4	0.5
	12	1	1.46	0.5
	13	1	1.52	0.5
	14	1	1.04	1
	15	1	1.08	1
	16	1	1.12	1

3. LGADs Fabrication

The LGADs and P-intrinsic-N (PIN) sensors used for these studies were produced by Fondazione Bruno Kessler (FBK) with the name Space LGADs for Astroparticle Physics (SLAPP). Using the simulations in Section 2 as a reference and the process parameters in Table 2, a total of 16 wafers with three thicknesses and several gain layers were fabricated. The goal was to achieve a gain of approximately 100. Over the last decade, the standard 50 μm sensors have been studied extensively for timing in HEP experiments. Due to their active thickness, they are produced on high-resistivity silicon grown epitaxially on a low-resistivity handle wafer. The 100 and 150 μm -thick sensors are realized using silicon-to-silicon bonded wafers, where a high resistivity wafer is bonded to a low resistivity handle wafer to allow for its thinning to the desired active thickness.

To study the effect of capacitance on the timing performance of the LGAD, pad sensors with three different dimensions were designed. Each wafer contains combinations of three different areas and three layouts for each area. The sensors have an active area of 6.25 mm^2 , 25 mm^2 , and 100 mm^2 . A guard ring structure was included to isolate the active area from the periphery of the sensor. In addition, to investigate the effect of n^+ layer's resistivity on timing performance, three different layouts were designed for each active area, as shown in Figure 3. Type-1 has no metallization on top and contacts between the metal and the n^+ are

placed along the perimeter of the device, Type-2 has the metallization and the same kind of contacts, while Type-3 has a matrix of contact openings between the metal and the n^+ layer, spread over the whole active area. The metallization on the latter two types has nine small openings of $100 \times 100 \mu\text{m}^2$ to allow laser light illumination.

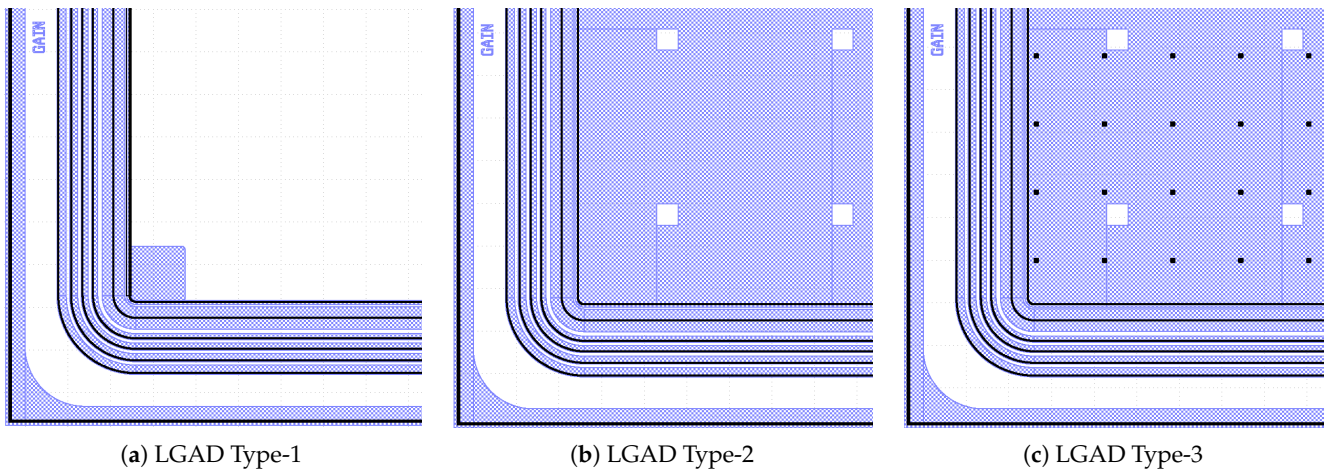


Figure 3. Schematics of the corner of LGAD layouts used in this study, where the metallization and the contacts with the n^+ layer are highlighted. Blue color represents the metal layer and the black color represents the contact between the metal and the n^+ layer.

4. Laboratory Measurements

A series of characterizations were conducted to make a comprehensive study of the SLAPP production. The leakage current, capacitance, gain, and jitter as a function of bias voltage were measured systematically. Additionally, the uniformity of response is also measured. The results are presented and discussed in the following subsections.

4.1. Leakage Current

Each wafer was incorporated with multiple test structures featuring both LGAD and PIN sensors of the same active area. To check the electrical properties of the sensors, current-voltage (IV) measurements were carried out on these using an automatic probe station at 24°C with and without illumination from an infrared LED of 930 nm. Figure 4 shows the comparison between the IV curves of 50, 100, and 150 μm -thick sensors represented by green, red, and blue colors, respectively. The IV measurements on the top panels (Figure 4a,b) are performed in dark conditions, whereas the ones on the bottom panels (Figure 4c,d) are under LED illumination. The devices with gain are featured on the left plots, while those without gain are depicted on the right.

The IV curves obtained from the PIN sensors do not exhibit any form of breakdown up to a bias voltage of 500 V. It is worth noting that the wafers with a thickness of 50 μm (shown in green) have the lowest leakage current among all wafers. As the wafer thickness increases, the leakage current also increases, which is an expected trend since a higher volume leads to a higher generation of charge carriers in the bulk. As for LGADs, it is possible to identify which fabrication parameters lead to early breakdown of the sensors, since their current exceeds $1 \mu\text{A}$ at a few tens of volts, even during the dark measurements. This breakdown is evident for wafers 7, 13, 15, and 16, attributed to the excessive doping of their gain layer. The 50 μm wafers also exhibit the least leakage current for LGADs, while for wafers with 100 and 150 μm thickness, there is not a uniform trend, although they are accompanied by a wider operating voltage range (see wafers 8, 11, and 12).

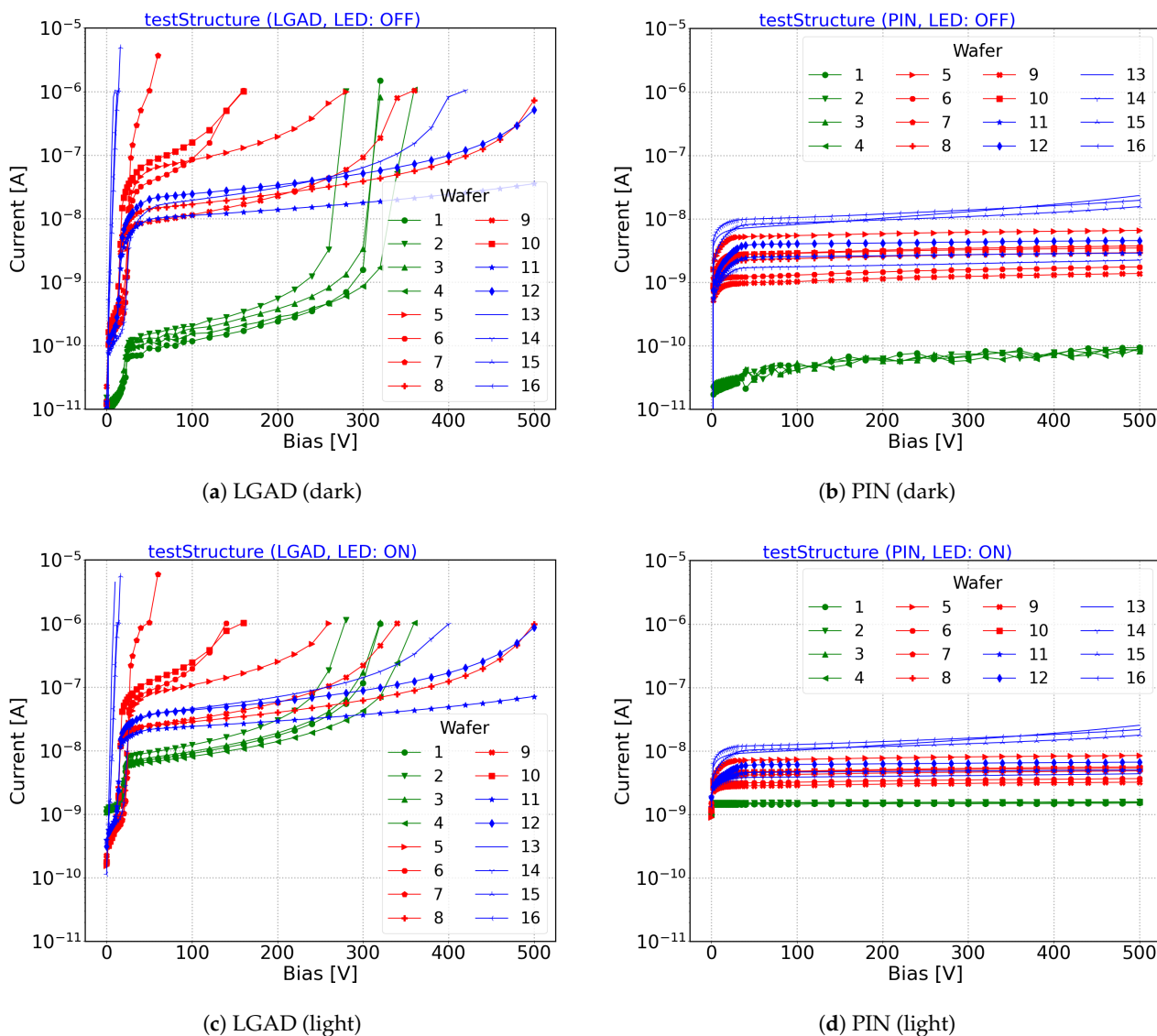


Figure 4. IV curves of PINs and LGADs with different thicknesses (represented by different colors) and different gain layer designs measured in the dark (a,b) and under low-intensity illumination (c,d). The devices with gain are shown on the left plots and those without gain on the right.

4.2. Capacitance

An LCR meter was utilized to measure the capacitance as a function of bias voltage up to a value for which the full depletion (V_{FD}) of the sensor is reached. The value of V_{FD} depends on the thickness and doping concentration of the wafer, and it is generally in the order of a few tens of volts. One wafer for each manufactured thickness was chosen for the test, among the promising ones arising from the previous IV characterization.

The left panel of Figure 5 illustrates the capacitance of 1 cm² LGAD sensors as a function of bias voltage for three different thicknesses and layout types. Different layouts are represented with different markers, while different thicknesses are displayed using different colors. For the three wafers, the gain layer depletion voltage is the one corresponding to the first knee of the curve: wafer 9 (in red) depletes earlier than wafer 1 (in green) and wafer 14 (in blue) depletes slightly later. The full depletion of the sensor is achieved at the bottom of the ankle when the capacitance becomes constant. Sensors from wafers 1 and 9 have a V_{FD} between 20 and 40 V, while it appears that wafer 14 fully depletes above 50 V (though it was not possible to verify this because of instrumental limitations). The

following trends are expected, according to the fabrication parameters (see Table 2): wafer 9 has lower implantation energy than wafer 1, thus it should deplete the gain layer earlier but should reach full depletion later because it is thicker; wafer 14 has the same implantation energy as wafer 1 so they deplete the gain layer almost at the same voltage.

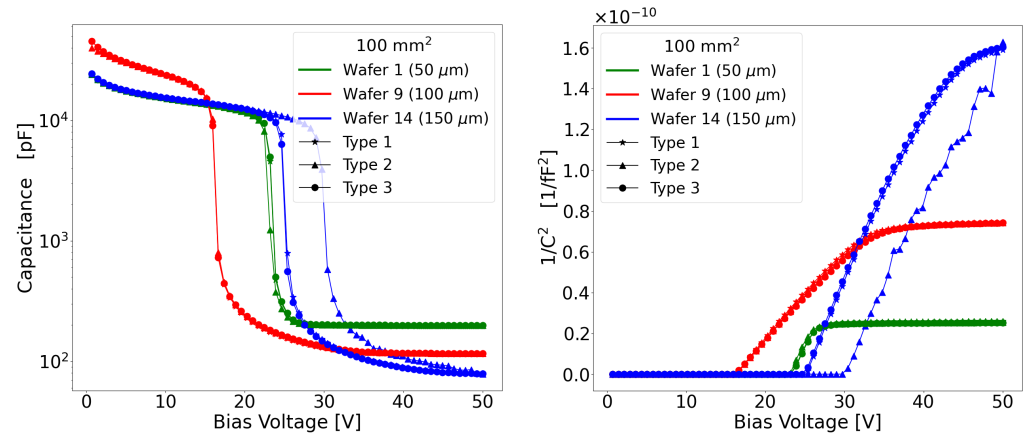


Figure 5. (Left) Capacitance of 100 mm² sensors as a function of bias voltage. The knee represents the gain layer depletion. (Right) 1/C² plot for the same sensors. The knee represents the full depletion voltage when the 1/C² value becomes constant.

4.3. Gain

The gain measurements are useful for the investigation of gain value and breakdown of the sensor due to the different gain layer designs. Utilizing the IV measurements outlined in Section 4.1, the gain can be calculated using the equation

$$Gain|_{LED} = \frac{(I_{light} - I_{dark})|_{LGAD}}{(I_{light} - I_{dark})|_{PIN}}, \quad (1)$$

where I_{light} is the current measured with the LED switched on and I_{dark} is with LED switched off. Figure 6 (Left) portrays the gain measurement as a function of bias voltage for all wafers, calculated from Equation (1). Wafers 13, 15, and 16 with 150 μm thickness (in blue) go into an early breakdown, indicating an overly doped gain layer, making the sensors in these wafers unusable. Wafers 6, 7, and 10 (in red) are the next to show a premature breakdown. As desired, the 50 μm-thick wafers, represented in green, maintain a consistent gain of $\mathcal{O}(10)$ at lower bias voltages and reach breakdown between 200 and 300 V. For the same bias voltage, the gain values of wafers 9 and 14 are larger than the 50 μm wafers, while wafers 8, 11, and 12 demonstrate a wider operating range, with a lower gain.

Individual sensors were mounted on a 16-channel readout board designed by Fermilab [22]; each channel features a two-stage amplifier capable of generating a uniform gain with 10% variation from channel to channel and a bandwidth of 1 GHz. These sensors were then tested with the Transient Current Technique (TCT) setup [23]. In TCT, an IR laser can simulate a Minimum Ionizing Particle (MIP) passing through the sensor. For this study, the IR laser was calibrated to 1 MIP and pulsed at 1 kHz. The triggered signal was then read out by the PCB and sent to an oscilloscope with 2.5 GHz bandwidth and 20 GS/s sampling rate for waveform digitization. The setup includes a beam monitor that continuously measures the laser intensity. The data from the beam monitor were used to normalize the sensors' charge to reduce the effect of laser fluctuations as much as possible.

The collected charge from sensors is measured by illuminating them with an IR laser and integrating the signal over time, which is then divided by the output impedance. An average of 256 waveforms is used in the oscilloscope to reduce noise fluctuations.

To estimate the gain of an LGAD, the charge for both an LGAD and a PIN sensor is estimated as a function of bias voltage. The gain is defined as

$$Gain|_{V_{bias}} = \frac{Q_{LGAD}}{Q_{PIN}} \Big|_{V_{bias}}, \tag{2}$$

where Q_{LGAD} and Q_{PIN} are the collected charge by the LGAD and PIN sensors, respectively. The gain measurements for 100 mm² LGADs are shown on the right panel of Figure 6 as a function of the bias voltage at room temperature. The error bars account for uncertainties arising from the amplifier response evaluated through repeated measurements of the same sensor, and the standard deviation amounts to 5% of the collected charge. The gain trend derived through this method is generally consistent with the gain measured from the test structures using LED, even though its value falls short of the 100 expected from simulations, reaching approximately 40. Simulation models used for impact ionization models often tend to provide inaccurate results, either underestimating or overestimating the gain values [24]. The impact ionization model used to estimate the gain values in this work tends to overestimate the gain. Different patterns are observed among sensors, even within the same wafer. In wafer 14, Type-3 has almost double the gain of Type-2; similarly, Type-2 of wafer 1 has a smaller gain than the other two. Since all three sensor types come from the same wafer, the different gain values can be explained by a non-uniformity in the implant dose of the gain layer.

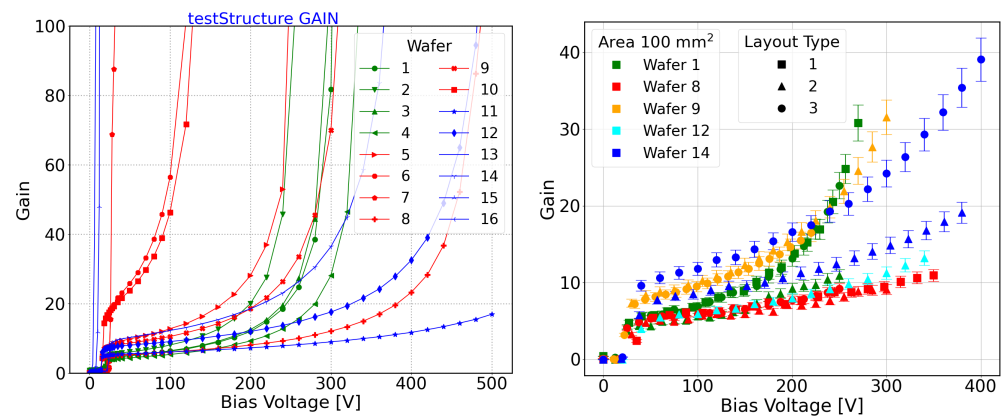


Figure 6. (Left) Gain of the wafers vs. bias voltage obtained from the IV measurement using Equation (1). (Right) Gain measurements using a pulsed IR laser impinging on 100 mm² pad sensors of different thicknesses, as a function of the bias voltage, calculated with Equation (2).

4.4. Time Resolution Study with Laser

The time resolution, σ_t , of a time-tagging detector can be described as a combination of four major factors,

$$\sigma_t^2 = \sigma_{TimeWalk}^2 + \sigma_{Landau}^2 + \sigma_{Jitter}^2 + \sigma_{TDC}^2, \tag{3}$$

where the first three terms originate from the signal crossing a threshold, while σ_{TDC} accounts for the uncertainty in time resolution due to the digital conversion of the signal in the readout electronics. The time walk arises since larger signals cross a fixed threshold value before the smaller signals, but it can be avoided using Constant Fraction Discrimination (CFD) as a time tagging method. The CFD algorithm sets the arrival time of the particle when the signal crosses a fixed threshold at a constant fraction of the signal amplitude. The production of eh pairs in a single event interaction and their distribution along the path is a stochastic process that gives rise to non-uniform charge deposition. This is called Landau noise, and σ_{Landau}^2 accounts for its effect. According to [25], the Landau contribution saturates towards a value less than 40 ps when the thickness of the silicon sensor is

increased over 70 μm ; however, it is not considered in this work. The focus of this work is on minimizing the σ_{jitter} term of Equation (3), which is caused by the presence of noise in the signal leading to the fluctuation in the crossing time at a specific threshold. For a given noise value, σ_{Noise} , in the system, the jitter can be expressed as follows:

$$\sigma_{\text{jitter}} = \frac{\sigma_{\text{Noise}}}{\text{Slew Rate } (dV/dt)} \propto \frac{\tau_{\text{rise}}}{\text{SNR}}. \quad (4)$$

Here, the slew rate represents the steepness of the signal, SNR is the signal-to-noise ratio, and τ_{rise} is the signal rise time.

To reduce jitter, one can either increase the SNR by increasing the signal using gain or decrease the noise in the sensor. The same TCT setup described in the previous subsection was used to measure the jitter of the LGADs. For each sensor, two measurements were conducted: the first aimed to quantify the slew rate by averaging 256 waveforms in the oscilloscope, while the second was dedicated to estimating the noise, involving no averaging. The jitter is calculated using Equation (4). The noise is defined as the standard deviation of fluctuations of the waveform around the baseline preceding the signal from the IR laser pulse, and it is presented as a function of bias voltage for the tested sensors in Figure 7. The average noise remains consistently below 2 mV across all wafers and areas, maintaining this level before the onset of breakdown. The lack of trend suggests the shot noise is not the dominant noise figure in the system. In the analysis presented herein, the slew rate was determined as the slope of the line that best fits the leading edge of the signal between 20% and 80% of signal amplitude.

Figure 8 shows the SNR, gain, rise time, and jitter for different active area pads from wafer 9 (100 μm thickness). The comparison reveals the impact of the sensor's active area on these parameters. When comparing sensors with the same layout, smaller active areas result in a steeper leading edge with higher amplitude in the signal shape, even though the collected charge is practically the same. This is due to the capacitance of the sensor, which scales linearly with the active area. As a direct consequence, smaller sensors exhibit better timing capabilities at the same bias voltage due to their lower rise time for a given gain.

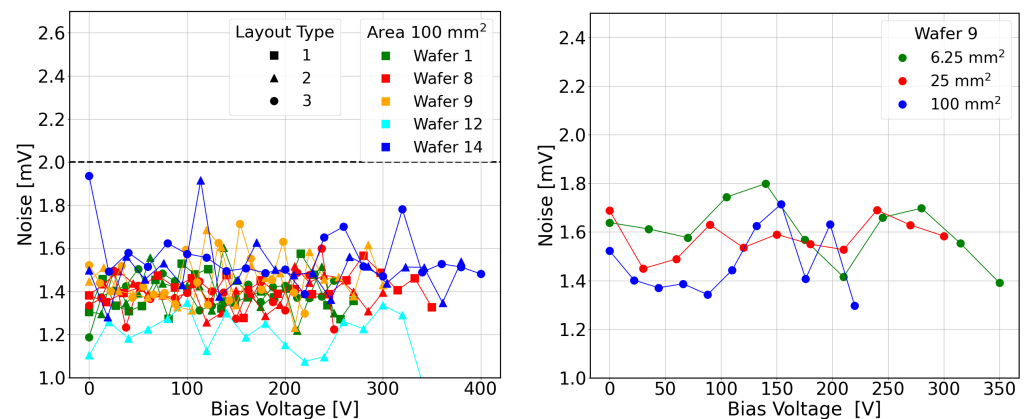


Figure 7. Noise as a function of the bias voltage across sensors of the same area (left), and of the same thickness 100 μm (right).

Focusing on the pads with the largest area, the dependence of jitter on both bias voltage and gain is depicted in Figure 9, highlighting the prospect of achieving sub-100 ps jitter levels with diverse gain layer designs, for sensors discussed in Section 4.3. From the plot on the left, it can be seen that wafers 9 (in orange) and 14 (in blue) are the only ones reaching lower values than the two threshold lines marking 100 ps (solid) and 50 ps (dashed), while wafer 12 goes below the first, making those the most promising designs. It is interesting to note that, after a certain gain value, the jitter saturates and will eventually shoot up if the gain is increased further due to the rise of shot noise. Among the 100 mm^2 sensors,

wafer 14 achieves the best jitter value of approximately 34 ps at 400 V when the gain is close to 40. However, wafer 9 achieves an equivalent value of jitter, i.e., 36 ps at 300 V and gain 32. The best performance is achieved for Type-2 and Type-3 layouts, which do not seem to show a significant difference once the gain of the different sensors is taken into account. These values show that thicker sensors require a higher bias voltage to achieve similar performance to thinner sensors because a higher bias voltage is required to achieve saturated velocities.

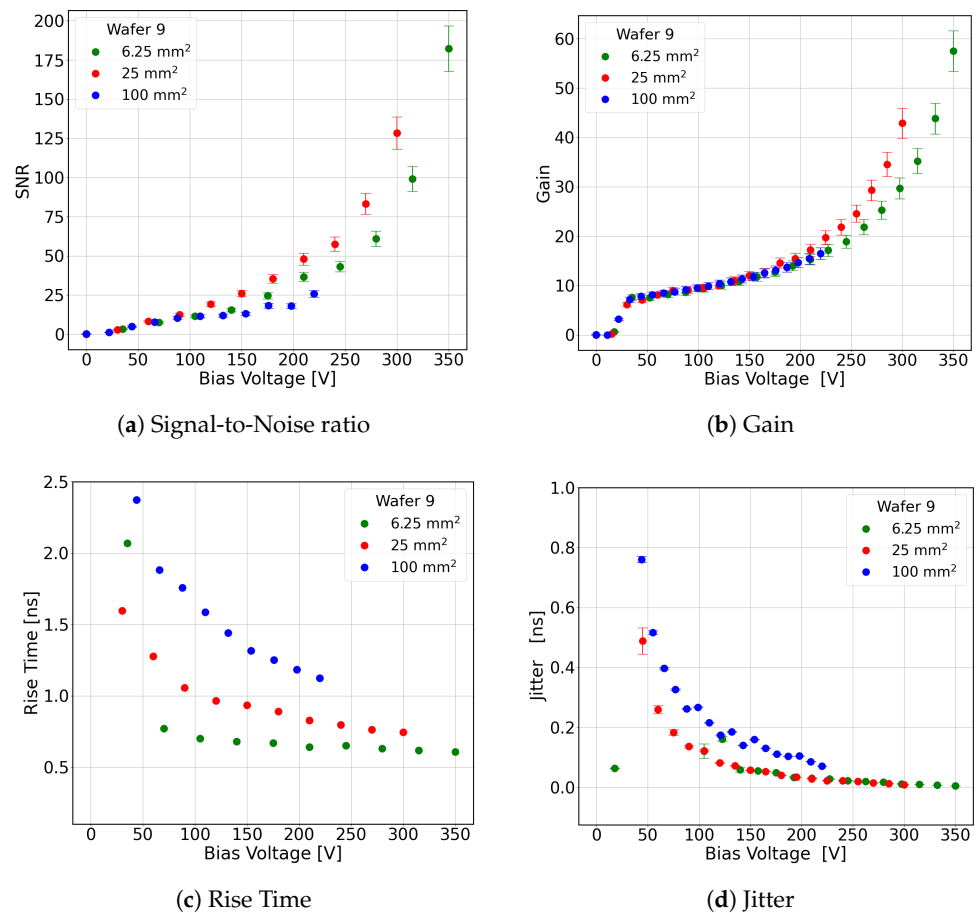


Figure 8. Different signal properties for all the active areas from wafer 9 (100 μm) sensors of Type-3 as a function of the bias voltage. The green, red, and blue represent 6.25, 25, and 100 mm² sensors, respectively.

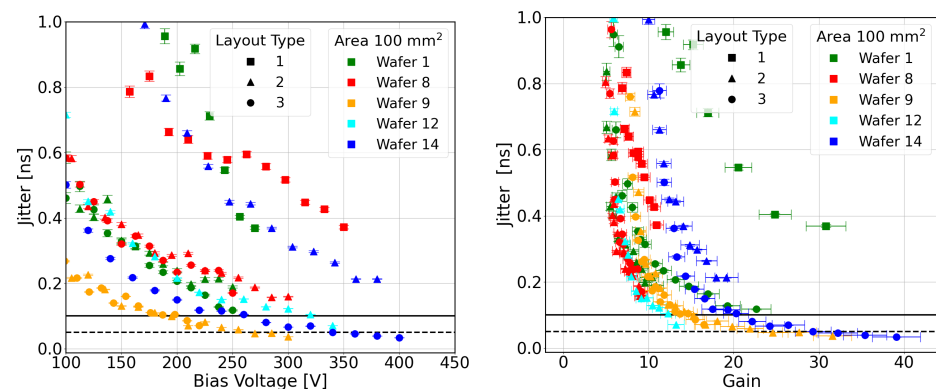


Figure 9. Performance of 100 mm² sensors from SLAPP production: (left) dependence of jitter on bias voltage, (right) jitter as a function of the gain to have a better comparison between the sensors' detection capabilities. The black solid and dashed lines denote the 100 and 50 ps values, respectively.

4.5. Uniformity

One of the issues to address with the large area sensors is the uniformity of signal shape across the active area. In LGADs, when a charged particle passes through the sensor the charge carriers are created, which then drift towards the electrodes. The movement of charge carriers induces the signal in the electrode. To examine the signal shape uniformity, the laser is used to create charge carriers at different distances from the position of the wire bond connecting the sensor to the readout electronics. The bond wire is placed close to a metal opening towards the edge of the sensor. The laser is shone on the sensor through different metal openings to observe variations in the arrival time of the sensor signal at the oscilloscope measured by a CFD algorithm with a threshold set at 50% of the signal amplitude. This measurement includes both the contribution of variation in the signal shape (different rise time) and in the signal propagation within the sensor.

Figure 10 illustrates the difference between the maximum and the minimum arrival times measured for both Type-2 and Type-3 sensors of wafer 9, with an active area of 100 mm². In the operating voltage region of the sensor, the spread remains constant while varying the bias voltage. The different values of Type-2 and Type-3 do not follow the expected trend from the layout design and need to be further investigated. For the Type-2 sensor, the contribution of the arrival time to the timing resolution is estimated as

$$\sigma_{uni} = \frac{153}{\sqrt{12}} \text{ ps} \approx 44 \text{ ps}, \quad (5)$$

where the numerator represents the mean value of arrival time spread and the denominator accounts for the assumption of a uniform distribution of particles on the detector. The spread obtained needs to be added to the jitter exhibited by the sensors when calculating the timing performances. The time resolution due to jitter and non-uniformity of the signal shape for the sensor with an active area of 100 mm² of wafer 9 Type-2 at 300 V is estimated as

$$\sigma_t = \sqrt{\sigma_{jitter}^2 + \sigma_{uni}^2} = \sqrt{36^2 + 44^2} \text{ ps} \approx 57 \text{ ps}. \quad (6)$$

This shows that the effect of non-uniformity plays a significant role in the timing performance of the larger sensors. In the application of this sensor in a tracking system, the effect of non-uniformity can be mitigated by correcting the measured arrival time using the reconstructed particle hit position.

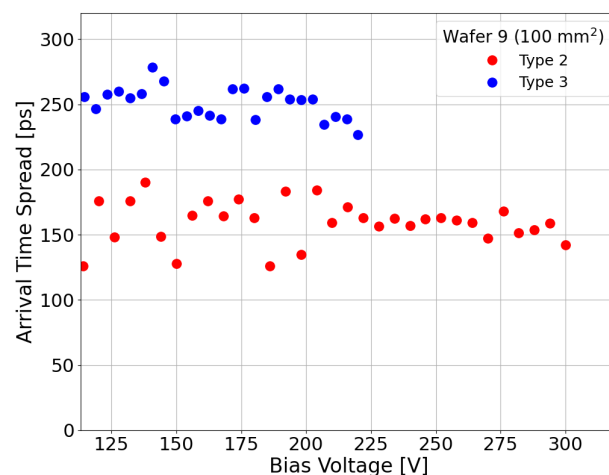


Figure 10. Spread in the arrival time of the signals generated in different positions across the sensor as a function of bias voltage for 100 mm² sensors from wafer 9. The values are calculated as the difference between the maximum and the minimum values of arrival time.

5. Summary and Conclusions

The findings of this research highlight the potential of LGADs as timing detectors in not only high energy physics but also in CCR experiments in space. The paper presents a new batch of LGADs with larger active areas and different thicknesses that have been produced and characterized in FBK. The outcomes of the work are summarized below:

- Electrical measurements (IV) for all the wafers with different gain layer designs indicate that the best gain layer designs to use see a dose of 1.46 and implantation energy of 0.5 for both 100 and 150 μm thicknesses, and a dose of 1.04 with an energy of 1 for 150 μm sensors. The other gain layer designs either go into an early breakdown or have too low a gain.
- A gain value of approximately 40 is achieved at 400 V for wafer 14. However, the LED measurements suggest that a gain of 100 is achievable at a bias voltage greater than 400 V, but the gain curve becomes steeper. If the gain curve is too steep, a small fluctuation in the operating voltage of the sensor will result in a different gain, making the operating condition of the device unstable.
- From the measurements using an IR laser with an intensity set to 1 MIP, a jitter of ~ 35 ps can be obtained on LGAD sensors with a 100 mm^2 area, with different design configurations.
- The uniformity of response of the sensors was measured using an IR laser. This effect's contribution to the sensors' time resolution is estimated to be 44 ps.

The study shows that LGAD sensors with an active area of 1 cm^2 have successfully achieved a jitter under 40 ps, and a time resolution estimated to be 60 ps when including non-uniformity effects, demonstrating the scalability of LGADs. Further optimization of the gain layer design is needed to have more gain at a lower bias voltage with a less steep gain curve, providing a larger range of bias with stable sensor operation. It is worth noting that this study does not consider the Landau fluctuations for these sensors, which is an important aspect that will be studied during tests with charged particles, foreseen in future studies.

Author Contributions: Conceptualization, A.B. and M.C.V.; data curation, A.B., L.C., F.C., O.H.A. and F.F.; formal analysis, A.B. and L.C.; investigation, A.B., L.C. and F.C.; project administration, M.B.; software, A.B., L.C. and M.C.V.; supervision, M.C.V., M.B. and G.P.; validation, L.C.; writing—original draft, A.B. and L.C.; writing—review and editing, A.B., L.C. and M.C.V. All authors have read and agreed to the published version of the manuscript.

Funding: This research received no external funding.

Institutional Review Board Statement: Not applicable.

Informed Consent Statement: Not applicable.

Data Availability Statement: The raw data supporting the conclusions of this article will be made available by the authors on request.

Acknowledgments: The authors would like to thank the people from Fermilab, Nicolò Cartiglia, and the Torino UFSD group, and ARTEL for designing the 16-channel Fermilab LGAD readout board.

Conflicts of Interest: The authors declare no conflicts of interest. The funders had no role in the design of the study; in the collection, analyses, or interpretation of data; in the writing of the manuscript; or in the decision to publish the results.

Abbreviations

The following abbreviations are used in this manuscript:

CCRs	Charged Cosmic Rays
CFD	Constant Fraction Discrimination
HEP	High-Energy Physics

LED	Light Emitting Diode
LGADs	Low-Gain Avalanche Diodes
MIP	Minimum Ionizing Particle
PIN	P-intrinsic-N
SLAPP	Space LGADs for Astroparticle Physics
SNR	Signal-to-Noise Ratio
TCT	Transient Current Technique

References

- Aguilar, M.; Alcaraz, J.; Allaby, J.; Alpat, B. The Alpha Magnetic Spectrometer (AMS) on the International Space Station: Part I—Results from the test flight on the space shuttle. *Phys. Rep.* **2002**, *366*, 331–405. [\[CrossRef\]](#)
- Aguilar, M.; Ali Cavasonza, L.; Ambrosi, G.; Arruda, L. The Alpha Magnetic Spectrometer (AMS) on the international space station: Part II—Results from the first seven years. *Phys. Rep.* **2021**, *894*, 1–116. [\[CrossRef\]](#)
- Tavani, M.; Barbiellini, G.; Argan, A.; Boffelli, F. The AGILE Mission. *Astron. Astrophys.* **2009**, *502*, 995–1013. [\[CrossRef\]](#)
- Atwood, W.B.; Abdo, A.A.; Ackermann, M.; Althouse, W. The Large Area Telescope on the Fermi Gamma-ray Space Telescope Mission. *Astrophys. J.* **2009**, *697*, 1071–1102. [\[CrossRef\]](#)
- Picozza, P.; Galper, A.; Castellini, G.; Adriani, O. PAMELA—A payload for antimatter matter exploration and light-nuclei astrophysics. *Astropart. Phys.* **2007**, *27*, 296–315. [\[CrossRef\]](#)
- Chang, J.; Ambrosi, G.; An, Q.; Asfandiyarov, R. The DARK MATTER PARTICLE Explorer mission. *Astropart. Phys.* **2017**, *95*, 6–24. [\[CrossRef\]](#)
- Alcaraz, J.; Alpat, B.; Ambrosi, G. A silicon microstrip tracker in space: Experience with the AMS silicon tracker on STS-91. *Il Nuovo Cimento A (1971–1996)* **1999**, *112*, 1325–1343. [\[CrossRef\]](#)
- Duranti, M.; Vagelli, V.; Ambrosi, G.; Barbanera, M.; Bertucci, B.; Catanzani, E.; Donnini, F.; Faldi, F.; Formato, V.; Graziani, M.; et al. Advantages and Requirements in Time Resolving Tracking for Astroparticle Experiments in Space. *Instruments* **2021**, *5*, 20. [\[CrossRef\]](#)
- Aplin, S.; Boronat, M.; Dannheim, D.; Duarte, J.; Gaede, F.; Ruiz-Jimeno, A.; Sailer, A.; Valantan, M.; Vila, I.; Vos, M. Forward tracking at the next e+e collider part II: Experimental challenges and detector design. *J. Instrum.* **2013**, *8*, T06001. [\[CrossRef\]](#)
- Pellegrini, G.; Fernández-Martínez, P.; Baselga, M.; Fleta, C.; Flores, D.; Greco, V.; Hidalgo, S.; Mandić, I.; Kramberger, G.; Quirion, D.; et al. Technology developments and first measurements of Low Gain Avalanche Detectors (LGAD) for high energy physics applications. *Nucl. Instrum. Meth.* **2014**, *A*, 12–16. [\[CrossRef\]](#)
- Cartiglia, N.; Staiano, A.; Sola, V.; Arcidiacono, R.; Cirio, R.; Cenna, F.; Ferrero, M.; Monaco, V.; Mulargia, R.; Obertino, M.; et al. Beam test results of a 16ps timing system based on ultra-fast silicon detectors. *Nucl. Instrum. Meth.* **2017**, *850*, 83–88. [\[CrossRef\]](#)
- Schael, S.; Atanasyan, A.; Berdugo, J.; Bretz, T. AMS-100: The next generation magnetic spectrometer in space—An international science platform for physics and astrophysics at Lagrange point 2. *Nucl. Instrum. Methods Phys. Res. Sect. A Accel. Spectrom. Detect. Assoc. Equip.* **2019**, *944*, 162561. [\[CrossRef\]](#) [\[PubMed\]](#)
- Kramberger, G.; Carulla, M.; Cavallaro, E.; Cindro, V.; Flores, D.; Galloway, Z.; Grinstein, S.; Hidalgo, S.; Fadeyev, V.; Lange, J.; et al. Radiation hardness of thin Low Gain Avalanche Detectors. *Nucl. Instrum. Methods Phys. Res. Sect. A Accel. Spectrom. Detect. Assoc. Equip.* **2018**, *891*, 68–77. [\[CrossRef\]](#)
- Analog Devices LTspice Official Website. Available online: <https://www.linear.com/LTspice> (accessed on 14 March 2022).
- Bichsel, H. Straggling in thin silicon detectors. *Rev. Mod. Phys.* **1988**, *60*, 663–699. [\[CrossRef\]](#)
- Dalla Betta, G.F.; Pancheri, L.; Boscardin, M.; Paternoster, G.; Piemonte, C.; Cartiglia, N.; Cenna, F.; Bruzzi, M. Design and TCAD simulation of double-sided pixelated low gain avalanche detectors. *Nucl. Instrum. Methods Phys. Res. Sect. A Accel. Spectrom. Detect. Assoc. Equip.* **2015**, *796*, 154–157. [\[CrossRef\]](#)
- Cividec Instrumentation. Available online: <https://cividec.at/index.php?module=public.product&idProduct=34&scr=0> (accessed on 21 September 2022).
- Teich, M.; Matsuo, K.; Saleh, B. Excess noise factors for conventional and superlattice avalanche photodiodes and photomultiplier tubes. *IEEE J. Quantum Electron.* **1986**, *22*, 1184–1193. [\[CrossRef\]](#)
- Scharf, C.; Klanner, R. Measurement of the drift velocities of electrons and holes in high-ohmic silicon. *Nucl. Instrum. Methods Phys. Res. Sect. A Accel. Spectrom. Detect. Assoc. Equip.* **2015**, *799*, 81–89. [\[CrossRef\]](#)
- SILVACO TCAD: Semiconductor Process and Device Simulation. Available online: <https://silvaco.com/tcad/> (accessed on 4 November 2022).
- Bisht, A. Development of Low Gain Avalanche Detectors for Astroparticle Physics Experiments in Space. Ph.D. Thesis, Univeristà degli Studi di Trento, Trento, Italy, 2023.
- Heller, R.; Abreu, A.; Apresyan, A.; Arcidiacono, R.; Cartiglia, N.; DiPetrillo, K.; Ferrero, M.; Hussain, M.; Lazarovitz, M.; Lee, H.; et al. Combined analysis of HPK 3.1 LGADs using a proton beam, beta source, and probe station towards establishing high volume quality control. *NIMA* **2021**, *1018*, 165828. [\[CrossRef\]](#)
- Large Scanning TCT Setup, Particulars. Available online: <http://particulars.si/index.php> (accessed on 7 June 2023).

24. Currás Rivera, E.; Moll, M. Study of Impact Ionization Coefficients in Silicon with Low Gain Avalanche Diodes. *IEEE Trans. Electron Devices* **2023**, *70*, 2919–2926. [[CrossRef](#)]
25. Siviero, F.; Arcidiacono, R.; Borghi, G.; Boscardin, M.; Cartiglia, N.; Vignali, M.C.; Costa, M.; Dalla Betta, G.-F.; Ferrero, M.; Ficorella, F.; et al. Optimization of the gain layer design of ultra-fast silicon detectors. *Nucl. Instrum. Methods Phys. Res. Sect. A Accel. Spectrom. Detect. Assoc. Equip.* **2022**, *1033*, 166739. [[CrossRef](#)]

Disclaimer/Publisher's Note: The statements, opinions and data contained in all publications are solely those of the individual author(s) and contributor(s) and not of MDPI and/or the editor(s). MDPI and/or the editor(s) disclaim responsibility for any injury to people or property resulting from any ideas, methods, instructions or products referred to in the content.